Influence of Metal Oxide Particles on Bandgap of 1D Photocatalysts Based on SrTiO$_3$/PAN Fibers

Fail Sultanov [1,2], Chingis Daulbayev [1,2,*], Seitkhan Azat [1,2,3,*], Kairat Kuterbekov [4,*], Kenzhebatyr Bekmyrza [4,*], Baglan Bakbolat [1,2,*], Magdalena Bigaj [5] and Zulkhair Mansurov [1,2]

[1] Faculty of Chemistry and Chemical Technology, al-Farabi Kazakh National University, Almaty 050000, Kazakhstan; sultanov.fail@kaznu.kz (F.S.); zmansurov@kaznu.kz (Z.M.)
[2] Laboratory of Energy-intensive and Nanomaterials, Institute of Combustion Problems, Almaty 050000, Kazakhstan
[3] Institute of Chemical and Biological Technologies, Satbayev University, Almaty 050000, Kazakhstan
[4] Faculty of Physics and Technology, L.N. Gumilev Eurasian National University, Nur-Sultan 010000, Kazakhstan
[5] NanoBioMedical Centre, Adam Mickiewicz University, 61-614 Poznan, Poland; magdalena.bigaj@amu.edu.pl
[*] Correspondence: chingis.daulbayev@kaznu.kz (C.D.); a.seitkhan@satbayev.university (S.A.); kuterbekov_ka@enu.kz (K.K.); bekmyrza_kzh@enu.kz (K.B.); bakbolat.baglan@icp.kz (B.B.)

check for updates

Abstract: This paper deals with the study of the optical properties of one-dimensional SrTiO$_3$/PAN-based photocatalysts with the addition of metal oxide particles and the determination of their bandgaps. One-dimensional photocatalysts were obtained by the electrospinning method. Particles of metals such as iron, chromium, and copper were used as additives that are capable of improving the fibers' photocatalytic properties based on SrTiO$_3$/PAN. The optimal ratios of the solutions for the electrospinning of fibers based on SrTiO$_3$/PAN with the addition of metal oxide particles were determined. The transmission and reflection of composite photocatalysts with metal oxide particles were measured in a wide range of spectra, from the ultraviolet region (185 nm) to near-infrared radiation (3600 nm), to determine the values of their bandgaps. Thus, the introduction of metal oxide particles resulted in a decrease in the bandgaps of the obtained composite photocatalysts compared to the initial SrTiO$_3$/PAN (3.57 eV), with the following values: -3.11 eV for SrTiO$_3$/PAN/Fe$_2$O$_3$, -2.84 eV for SrTiO$_3$/PAN/CuO, and -2.89 eV for SrTiO$_3$/PAN/Cr$_2$O$_3$. The obtained composite photocatalysts were tested for the production of hydrogen by the splitting of water–methanol mixtures under UV irradiation, and the following rates of hydrogen evolution were determined: 344.67 µmol h^{-1} g^{-1} for SrTiO$_3$/PAN/Fe$_2$O$_3$, 398.93 µmol h^{-1} g^{-1} for SrTiO$_3$/PAN/Cr$_2$O$_3$, and 420.82 µmol h^{-1} g^{-1} for SrTiO$_3$/PAN/CuO.

Keywords: electrospinning; SrTiO$_3$; fibers; photocatalytic; water splitting; bandgap; hydrogen

1. Introduction

Photocatalysis is a well-researched method for renewable energy production in the forms of solar energy and high-purity chemical fuel (H$_2$, CH$_4$/CH$_2$OH) [1,2]. Photocatalytic water splitting occurs upon the solar light irradiation of a semiconductor photocatalyst and results in the formation of hydrogen (H$_2$) and oxygen (O$_2$) [3]. An advantage over conventional energy sources, like fossil fuels, is the lack of carbon monoxide production, which, in light of ongoing climate change debates, is a great benefit for the environment [4].

The material used in the photocatalytic system has to be chosen carefully. Strontium titanate ($SrTiO_3$) is a wide-gap semiconductor that belongs to the perovskite family of ternary oxides with an ABO_3 structure [5]. At room temperature, it exhibits a cubic structure with a lattice parameter a = 3.9053 Å [6]. Its attractive properties include strong catalytic activity, high chemical stability, and the long lifetime of electron-hole pairs [5]. Due to the bandgap energy of 3.2 eV, photo-excitation takes place with the use of light with a wavelength λ less than 387 nm (UV light) [2,7], which accounts for about 5% of solar energy [8]. The inherent gap edge positions can be modified by the implementation of elemental doping in the original semiconductor material [5,9]. Doping with metal or non-metal alloys can be applied to extend the activating spectrum, allowing the $SrTiO_3$ photocatalyst to also be used in the visible light region [7,9]. Metal ions implemented in the semiconductor material become electron donors, enhancing the production of hydrogen [3,8,9]. Transition metal ions like Fe, Mn, Cu, Ni, and Cr have been shown to modify the bandgap position of semiconductor materials [10–15] without enhancing the formation of water, which is the case when noble metals (e.g., Rh, Pt) are employed [3,9]. The switch towards the visible light region was also achieved by doping titanate-based materials with Fe [9,16,17], Cr [5,18–20], and Cu [21,22].

The presence of metal in the semiconductor lattice alters electron-hole recombination. Since the transfer of the trapped electron and hole to the semiconductor surface is required for the photocatalytic reaction to occur, it is important that the metal ions are located near the surface of the semiconductor for a more efficient charge transfer [9]. In addition, the effective separation of charges is significantly affected by the specific surface area, which promotes the free diffusion of water [23], as well as the high degree of crystallinity of photocatalysts, leading to a decrease in the number of recombinations of photogenerated charges [24]. Moreover, for the successful use of photocatalysts for the production of hydrogen by water splitting, it is necessary to develop and create inexpensive, efficient, and stable photocatalytic systems, which can result in a decrease in the market price of hydrogen [25].

In our previous work, we reported a low-cost synthesis and thorough characterization of $SrTiO_3$ nanofibers (up to 350 nm in diameter) using the electrospinning method [26]. Here, we show that the modification of this material using oxides of particles of iron (Fe), chromium (Cr), and copper (Cu) results in a narrowing of the bandgap energy. The used metal oxides have different properties for trapping and transferring electrons and holes. An increase in the efficiency of the hydrogen evolution reaction from the water-alcohol mixture under visible light irradiation (λ > 400 nm), without disrupting the nanofibers, structure, or crystallinity of $SrTiO_3$, was observed for all of the metal oxide particles added to $SrTiO_3$ nanofibers. The results of this work show that metal oxide particles added to $SrTiO_3$ nanofibers create visible-light-responsive photocatalysts, making them potent candidates for the conversion of solar energy to fuel.

2. Materials and Methods

Strontium nitrate ($Sr(NO_3)_2$, 98%), titanium oxide (TiO_2, 99%), and oxalic acid ($(COOH)_2 \cdot 2H_2O$, 98%) were purchased from Laborpharma (Almaty, Kazakhstan). Polyacrylonitrile (PAN, average M.W. is 152000), dimethylformamide (99.8%), iron chloride ($FeCl_3$, 45% solution), copper oxide (CuO, 99.995% powder), and chromium sulfate ($Cr_2(SO_4)_3$, 99.99% powder) were purchased from Sigma Aldrich (St. Louis, MO, USA). All chemicals were used without further purification.

2.1. Electrospinning of $SrTiO_3$/PAN-Based Fibers with the Addition of Metal Oxide Particles

$SrTiO_3$ was obtained as described in [27]. A precursor for the electrospinning of fibers based on $SrTiO_3$ and metal oxide particles was prepared as follows: PAN was used to create the polymer solution by its dissolution in dimethylformamide under constant stirring for 30 min. Then, $SrTiO_3$ powder and $FeCl_3$, $Cr_2(SO_4)_3$, or CuO were added to the polymer solution at different ratios and stirred until the mixture became homogeneous. The obtained suspension was used as a precursor for obtaining fibers based on $SrTiO_3$ with metal oxide particles by pulling under high voltage. Fiber

electrospinning was carried out at room temperature with a voltage of 16 kV and a flow rate of 1.5 mL/h. The collector was located at a distance of 15 cm from the needle. Aluminum foil with a 20 cm diameter was used as a collector, which was replaced every 1.5 h throughout the entire process. The obtained fibers were then thermally stabilized at 185 °C for 15 min and calcined at 500 °C for 30 min in an argon medium. The resulting samples were designated as $SrTiO_3/PAN/Fe_2O_3$, $SrTiO_3/PAN/CuO$, and $SrTiO_3/PAN/Cr_2O_3$ depending on the added metal.

2.2. X-ray Diffraction Analysis of Samples

The X-ray diffraction (XRD) analysis was carried out on a Dron-4-type X-ray diffractometer (Omsk, Russian Federation) with a range of rotation angles for diffraction unit detection from −100° to 168°. The minimum step for moving the detection unit is 0.001°. The permissible connection of the detection unit from a given rotation angle is ± 0.015°. The transport rate of the goniometer is 820°/min. The main error in measuring the pulse count of the X-ray measurement was not more than 0.4%.

2.3. Scanning Electron Microscope Characterization of the Surface Morphology of Samples

The surface morphology of the obtained photocatalytic fibers was studied using a Quanta 3D 200i (Waltham, MA, USA) scanning electron microscope (SEM) under an accelerating 15 kV voltage.

2.4. Measurement of the Transmission and Reflection of SrTiO_3/PAN Fibers with the Addition of Metal Oxide Particles in a Wide Spectral Region from Ultraviolet (185 nm) to Near-Infrared Radiation (3600 nm)

The transmission and reflection measurements of photocatalytic fibers with the addition of metal oxide particles in a wide spectral region, from ultraviolet (185 nm) to near-infrared radiation (3600 nm), were carried out on a Shimadzu UV-3600 spectrophotometer (Moscow, Russian Federation) equipped with three detectors: a photoelectron multiplier for operation in the ultraviolet and visible spectral range, a semiconductor InGaAs, and cooled PbS detectors for near-infrared operation.

2.5. Investigation of the Activity of Photocatalysts Based on SrTiO_3/PAN Fibers with the Addition of Metal Oxide Particles

The activity of photocatalysts based on $SrTiO_3/PAN$ fibers with the addition of metal oxide particles was tested by measuring the output of hydrogen during the water–methanol mixture splitting under UV radiation. The mixture, containing a photocatalyst, water, and methanol in different ratios, was loaded into a quartz tube reactor, which was previously purged with inert gas (argon) and exposed to UV irradiation with a wavelength of 320 nm and a power source of 40 W. As a result of the photocatalytic reaction of the water–methanol mixture splitting, the evolved mixture of gases was accumulated in a sealed sampler. The qualitative and quantitative composition of the evolved mixture of gases was analyzed by gas chromatography on a Chromos 1000 chromatograph (Dzershinsk, Russian Federation) with three packed 3 mm columns filled with NAX and PORAPAK Q phases, allowing for the identification of the leading gases: hydrogen, nitrogen, oxygen, carbon monoxide, and carbon dioxide.

3. Results and Discussion

3.1. The Synthesis of Fibers Based on SrTiO_3/PAN with the Addition of Metal Oxide Particles and a Study of Their Physicochemical Properties

To achieve a highly efficient photocatalyst based on $SrTiO_3$ fibers, it is necessary to create its composites with metal oxide particles. The addition of metal oxide particles allows for a narrowing of the bandgap of $SrTiO_3$, leading to the possible use of a wide spectrum of visible light. It also contributes to the improvement of redox reactions that occur during the absorption of light. The experimentally selected optimal ratios of the solution components for obtaining fibers with the required characteristics

are 1:9:2:88 $SrTiO_3$:PAN:$FeCl_3$:solvent, 0.5:10:1.5:88 $SrTiO_3$:PAN:$Cr_2(SO_4)_3$:solvent, and 1.5:8:2.5:88 $SrTiO_3$:PAN:CuO:solvent.

　　　Figure 1 presents SEM images of the obtained polymer fibers based on $SrTiO_3$/PAN with metal oxide particles added. Polymer fibers based on $SrTiO_3$/PAN with the addition of metal oxide particles have a continuous cylindrical shape without defects and are randomly arranged. The samples have the typical structure of fibers obtained by electrospinning, in which they are in contact with each other, forming a three-dimensional polymer network [28]. The average diameter of the obtained fibers is in the range from 200 to 400 nm, which is directly proportional to the viscosity of the solution used for electrospinning and the high voltage applied [29]. According to the SEM images, the presence of metal oxide particles and $SrTiO_3$ does not affect the morphological characteristics of the forming polymer fibers, which is also confirmed by the results obtained in [30], in which the effect of the composition of the electrospinning solution on the diameters of such fibers was studied. For all types of obtained fibers, the size of the agglomerates of $SrTiO_3$ and metal oxides ranges from 1 to 4 µm.
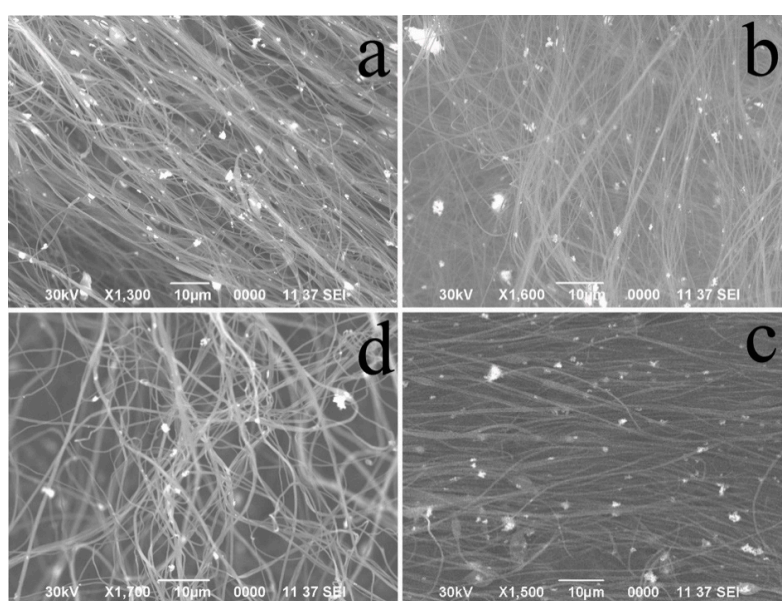

Figure 1. SEM images of non-calcined polymer fibers based on $SrTiO_3$/PAN (**a**) and their composites with metal oxide particles: $SrTiO_3$/PAN/Fe_2O_3 (**b**), $SrTiO_3$/PAN/Cr_2O_3 (**c**), and $SrTiO_3$/PAN/CuO (**d**).

　　　The inclusion of metal oxides does not cause a corresponding change in the fiber diameter. On the one hand, the metal particle addition increases the viscosity of the solution, but on the other hand, this effect is balanced by an increase in the electrical conductivity of the initial solution, which contributes to the formation of thinner fibers due to an increase in the charge density on the electrospinning jet, and this, in turn, leads to an elongation of the jet along its axis [31,32].

　　　To confirm the presence of metal oxide particles in the calcined fiber structure based on $SrTiO_3$/PAN, an XRD analysis of the samples was performed. Figure 2 presents the X-ray diffraction patterns of calcined fibers based on $SrTiO_3$/PAN and their composites with metal oxide particles.

　　　Figure 2a shows that for calcined $SrTiO_3$/PAN-based fibers, characteristic peaks are observed at 22.77°, 32.41°, 39.99°, 46.49°, 57.81°, 67.86°, and 77.17°, indicating the presence of perovskite-type $SrTiO_3$ in the structure. These peaks are also present in the X-ray diffraction patterns for samples of $SrTiO_3$/PAN with the addition of metal oxide particles (Figure 2b), indicating the presence of $SrTiO_3$ in each sample (JCPDS:35-0734). At the same time, for samples of $SrTiO_3$/PAN with the addition of metal oxide particles, peaks with a lower intensity are also observed: for Fe_2O_3, the characteristic peaks are at 33.14°, 35.68°, 49.51°, 52.34°, and 54.07°; for Cr_2O_3, they are at 22.79°, 24.50°, 33.66°, 36.25°, 41.58°, 63.54°, and 65.24°; and for CuO, they are at 22.74°, 35.46°, 36.46°, 38.66°, and 52.32°

(Figure 2b). According to the XRD analysis, for the $SrTiO_3/PAN/Fe_2O_3$ sample, the content of $SrTiO_3$ in the fibers is 89.6 wt.%, while the content of Fe_2O_3 is 10.4 wt.% (Figure 2b, black line). The crystal lattice parameter for $SrTiO_3$ is 3.9036 Å (for the standard compound, it is 3.90010 Å), indicating a good crystallinity of the obtained samples of calcined fibers based on $SrTiO_3/PAN/Fe_2O_3$. The crystallite size of the $SrTiO_3/PAN/Fe_2O_3$ composite is 740 Å. Figure 2b (red line) presents the X-ray diffraction pattern of calcined fibers based on $SrTiO_3/PAN/Cr_2O_3$; the content of $SrTiO_3$ in the structure is 54.3 wt.%, while the content of Cr_2O_3 is 45.7 wt.%. The higher content of Cr_2O_3 compared to Fe_2O_3 is associated with the molar masses and densities of $Cr_2(SO_4)_3$ and $FeCl_3$, which were used as additives in the process of electrospinning the composite fibers. The molar volume of $Cr_2(SO_4)_3$ is twice as high as that of $FeCl_3$, which is confirmed by the semi-quantitative analysis of the calcined fibers based on $SrTiO_3/PAN/Cr_2O_3$ and $SrTiO_3/PAN/Fe_2O_3$. The crystallite size for fibers based on $SrTiO_3/PAN/Cr_2O_3$ is 840 Å, and the crystal lattice parameter for $SrTiO_3$ is 3.9036 Å. According to the results of the XRD analysis of the calcined fibers based on $SrTiO_3/PAN /CuO$ (Figure 2b, blue line), the content of $SrTiO_3$ is determined to be 77.8 wt.%, and the content of CuO is 21.2 wt.% The crystallite size for the fiber based on $SrTiO_3/PAN/CuO$ is 760 Å.
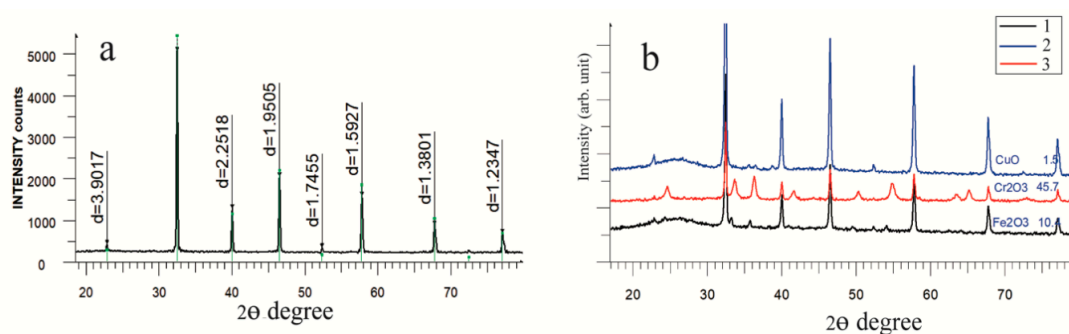

Figure 2. X-ray diffraction patterns of calcined fibers based on $SrTiO_3/PAN$ (**a**) and $SrTiO_3/PAN$ with the addition of metal oxide particles (**b**): $SrTiO_3/PAN/Fe_2O_3$—1 (black line); $SrTiO_3/PAN/CuO$—2 (blue line); $SrTiO_3/PAN/Cr_2O_3$—3 (red line).

3.2. Investigation of the Transmission and Reflection Spectra of the Obtained Photocatalytic Fibers

The photocatalysis mechanism of $SrTiO_3$ is based on the formation of electron–hole pairs under UV irradiation, where they have sufficiently high energy for the formation of radicals with a high oxidation ability. To study the possible use of a wider spectrum, including visible light, for $SrTiO_3/PAN$-based photocatalysts with the addition of metal oxide particles, their transmission and reflection spectra were determined. Analysis of the transmission spectra allows for the calculation of the bandgap of $SrTiO_3$-based photocatalysts with the addition of metal oxides. For crystalline semiconductors, the following equation is valid for the relationship between the absorption coefficient and the incident photon's energy:

$$\alpha(\vartheta)h\vartheta = B\ (h\vartheta - E_{gap})^m \qquad (1)$$

where E_{gap} is the optical bandgap, B is a constant, $h\vartheta$ is incident photon energy, and $\alpha(\upsilon)$ is an absorption coefficient, which is in accordance with the law of Beer–Lambert, equal to

$$\alpha(\vartheta) = 2303Ab(\lambda)/d \qquad (2)$$

where d is film thickness and $Ab(\lambda)$ is the film absorption coefficient.

For a more accurate determination of α, a correction that accounts for the reflection spectrum for the absorption coefficient must be made. To calculate the bandgap of $SrTiO_3/PAN$-based photocatalysts with the addition of metal oxide particles, it is necessary to rewrite Equation (1):

$$\alpha(\vartheta) = B(hc)^{(m-1)}\lambda(1/\lambda - 1/\lambda_g)^m \qquad (3)$$

where λ_g is the wavelength corresponding to the bandgap, h is the Planck constant, and c is the speed of light.

Using the Beer–Lambert law, Equation (3) can be rewritten as follows:

$$Ab(\lambda) = B(hc)^{(m-1)}d/2303(1/\lambda - 1/\lambda_g)^m + B_1 \tag{4}$$

where B_1 is the constant that takes into account the reflection spectrum.

Using Equation (4), the optical bandgap can be calculated by fitting the absorption spectrum without considering the film thickness. To determine the bandgap (E_{gap}), the absorption coefficient's dependence on the incident radiation energy was plotted and a linear approximation was carried out. Figure 3 presents the absorption and reflection spectra (Figure 3a) and a graph of the absorption coefficient's dependence on the incident radiation energy for SrTiO$_3$/PAN-based photocatalysts with the addition of metal oxide particles (Figure 3b).
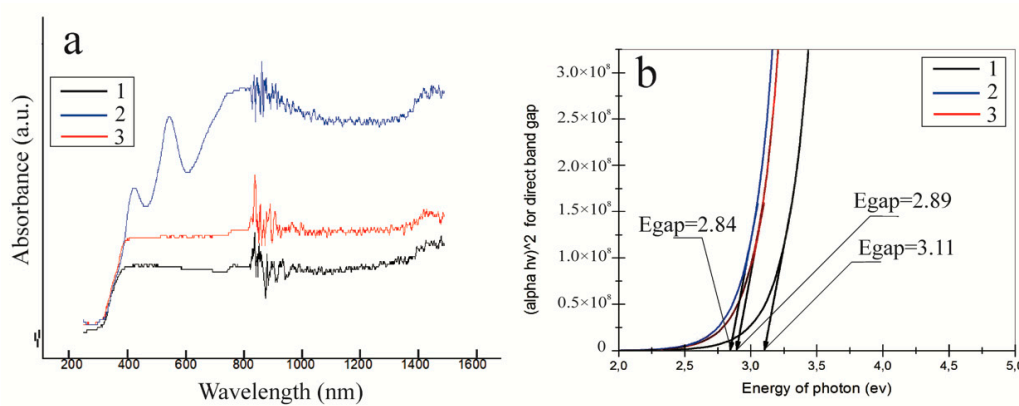

Figure 3. Absorption and reflection spectra (**a**) and values of the bandgap (**b**) of synthesized composite photocatalysts: SrTiO$_3$/PAN/Fe$_2$O$_3$—1 (black line); SrTiO$_3$/PAN/CuO—2 (blue line); and SrTiO$_3$/PAN/Cr$_2$O$_3$—3 (red line).

As a result, the bandgap for SrTiO$_3$/PAN-based photocatalysts with Cr$_2$O$_3$ particles added is determined to be 2.89 eV (Figure 3b, red line). Thus, it is found that the addition of Cr$_2$O particles to SrTiO$_3$-based fibers narrows the bandgap to 2.89 eV, making it possible to use a wide radiation spectrum. The determined value of the bandgap for a SrTiO$_3$/PAN-based photocatalyst with Cr$_2$O$_3$ particles added can be explained by the occupied level of Cr^{3+} cations, which is 1.0 eV above the valence band. The bandgap of the SrTiO$_3$/PAN-based photocatalyst with CuO particles added is 2.84 eV (Figure 3b, blue line). The determined bandgap of the SrTiO$_3$/PAN-based photocatalyst with the addition of Fe$_2$O$_3$ particles is 3.11 eV (Figure 3b, black line). A high bandgap value for a photocatalyst with Fe$_2$O$_3$ particles added is associated with a low Fe$_2$O$_3$ content in calcined fibers, confirmed by XRD (Figure 1b, black line). In turn, the calculated bandgap of the photocatalyst based on the initial SrTiO$_3$/PAN fibers without metal oxide particles added is 3.57 eV.

3.3. Investigation of the Activity of Photocatalysts Based on SrTiO$_3$/PAN Fibers with the Addition of Metal Oxide Particles by the Output of Hydrogen during the Splitting of Water–Methanol Mixture

After determining the bandgaps of photocatalysts based on SrTiO$_3$/PAN fibers with the addition of metal oxide particles, their photocatalytic efficiencies in the splitting of water–methanol mixtures with the production of hydrogen were studied. As seen in Table 1, the composition of the photocatalyst significantly affects the efficiency of hydrogen evolution. As reported in previous work [26], the photocatalytic hydrogen evolution rate from the splitting of the water-methanol mixture using SrTiO$_3$/PAN-based fibers at a 40W UV radiation is 305.96 µmol/h. In turn, the results of the measurement of the average rate of hydrogen evolution during the splitting of the water–methanol mixture at 400W UV irradiation of the composite SrTiO$_3$/PAN-based fibers with the addition of metal oxides are the following:

344.67 μmol/h for the $SrTiO_3/PAN/Fe_2O_3$ photocatalyst, 398.93 μmol/h for the $SrTiO_3/PAN/Cr_2O_3$ photocatalyst, and 420.82 μmol/h for the $SrTiO_3/PAN/CuO$ photocatalyst. The higher rates of hydrogen evolution for photocatalysts based on $SrTiO_3/PAN$ fibers with metal oxides added are explained by the fact that the optical, thermal, and electrochemical properties of metal oxide particles, which also highly depend on their sizes, allow not only for a narrowing of the bandgap of the semiconductors used as a photocatalyst but also for an improvement of their ultraviolet absorption ability.

Table 1. Comparison of the photocatalytic activity of different photocatalysts for producing hydrogen by splitting mixtures of water and alcohol.

Type of Photocatalyst	Parameters of the Process	Composition of the Water Mixture	The Output of Hydrogen, $\mu mol\ h^{-1}\ g^{-1}$	Reference
$SrTiO_3/PAN$-based fibers	40 W UV lamp, quartz reactor	80% of water and 20% of CH_3OH	305.96	[26]
$SrTiO_3/PAN/Fe_2O_3$ fibers	40 W UV lamp, quartz reactor	80% of water and 20% of CH_3OH	344.67	This work
$SrTiO_3/PAN/Cr_2O_3$ fibers	40 W UV lamp, quartz reactor	80% of water and 20% of CH_3OH	398.93	This work
$SrTiO_3/PAN/CuO$ fibers	40 W UV lamp, quartz reactor	80% of water and 20% of CH_3OH	420.82	This work
$MoSe_2/TiO_2$	Xe arc lamp	90% of water and 10% of CH_3OH	4.9	[33]
$SrTiO_3$ doped with Cr and N	300 W xenon lamp, quartz reactor	81.5% of water and 18.5% of CH_3OH	106.7	[34]
Pt/TiO_2	125 W xenon lamp, quartz reactor	70% of water and 30% of CH_3OH	523.71	[35]
$Pt/ZrO_2/TaO_n$	300 W mercury lamp, quartz reactor	85% of water and 15% of CH_3OH	9	[36]

A comparison of the photocatalytic activity of different photocatalysts for hydrogen production shows that the composition of the photocatalyst and the type and intensity of irradiation significantly influence the intensity of hydrogen evolution. The rate of photocatalytic hydrogen evolution from a water–organic alcohol mixture using $SrTiO_3/PAN$-based fibers with the addition of metal oxide particles during UV radiation with 40 W power is several times higher than that of reference analogs [32–36]. Moreover, irradiation with a power of 300 to 400 W was used in these works, which is not economically profitable, in contrast to lamps with a power of 40 W. In [34], TiO_2 doped with platinum particles was used as a photocatalyst. The power of ultraviolet radiation was 125 W, and the rate of photocatalytic hydrogen evolution using this photocatalyst with platinum was 523.71 μmol/h, which is still comparable to the hydrogen evolution rate for the $SrTiO_3/PAN/CuO$-based photocatalyst, while the cost and applied irradiation power required to conduct photocatalysis are much lower.

4. Conclusions

One-dimensional photocatalysts based on $SrTiO_3/PAN$ fibers with the addition of metal oxide particles were obtained by the electrospinning method. A study of the transmission and reflection spectra showed that the addition of Cr_2O_3, CuO, and Fe_2O_3 particles led to decreases in the bandgaps of $SrTiO_3/PAN$-based photocatalysts to 2.89, 2.84, and 3.11 eV, respectively. As a result of the addition of metal oxide particles to the initial $SrTiO_3/PAN$-based photocatalyst, the rate of hydrogen evolution in the photocatalytic splitting of a water–methanol mixture increased to 344.67 $\mu mol\ h^{-1}\ g^{-1}$ for the photocatalyst based on $SrTiO_3/PAN/Fe_2O_3$, 398.93 $\mu mol\ h^{-1}\ g^{-1}$ for the photocatalyst based on $SrTiO_3/PAN/Cr_2O_3$, and 420.82 $\mu mol\ h^{-1}\ g^{-1}$ for the photocatalyst based on $SrTiO_3/PAN/CuO$. We believe that this article's proposed approach for increasing the efficiency of photocatalysts by the addition of non-expensive materials, allowing for a reduction in their bandgap, is a promising method for the further development of technologies for efficient solar hydrogen production.

References

1. Shtarev, D.S.; Shtareva, A.V.; Kevorkyants, R.; Rudakova, A.V.; Molokeev, M.S.; Bakiev, T.V.; Bulanin, K.M.; Ryabchuk, V.K.; Serpone, N. Materials synthesis, characterization and DFT calculations of the visible-light-active perovskite-like barium bismuthate $Ba_{1.264(4)}$ $Bi_{1.971(4)}O_4$ photocatalyst. *J. Mater. Chem. C* **2020**, *8*, 3509–3519. [CrossRef]

2. Zhang, X.; Fu, A.; Chen, X.; Liu, L.; Ren, L.; Tong, L.; Ye, J. Highly efficient Cu induced photocatalysis for visible-light hydrogen evolution. *Catal. Today* **2019**, *335*, 166–172. [CrossRef]

3. Ismail, A.A.; Bahnemann, D.W. Photochemical splitting of water for hydrogen production by photocatalysis: A review. *Sol. Energy Mater. Sol. Cells* **2014**, *128*, 85–101. [CrossRef]

4. Sultanov, F.R.; Daulbayev, C.; Bakbolat, B.; Mansurov, Z.A.; Urazgaliyeva, A.A.; Ebrahim, R.; Pei, S.S.; Huang, K.-P. Microwave-enhanced chemical vapor deposition graphene nanoplatelets-derived 3D porous materials for oil/water separation. *Carbon Lett.* **2020**, *30*, 81–92. [CrossRef]

5. Phoon, B.L.; Lai, C.W.; Juan, J.C.; Show, P.-L.; Pan, G.-T. Recent developments of strontium titanate for photocatalytic water splitting application. *Int. J. Hydrogen Energy* **2019**, *44*, 14316–14340. [CrossRef]

6. Collignon, C.; Lin, X.; Rischau, C.W.; Fauqué, B.; Behnia, K. Metallicity and superconductivity in doped strontium titanate. *Annu. Rev. Condens. Matter Phys.* **2019**, *10*, 25–44. [CrossRef]

7. Xu, B.; Ahmed, M.B.; Zhou, J.L.; Altaee, A. Visible and UV photocatalysis of aqueous perfluorooctanoic acid by TiO_2 and peroxymonosulfate: Process kinetics and mechanistic insights. *Chemosphere* **2020**, *243*, 125366. [CrossRef]

8. Sinhmar, A.; Setia, H.; Kumar, V.; Sobti, A.; Toor, A.P. Enhanced photocatalytic activity of nickel and nitrogen codoped TiO_2 under sunlight. *Environ. Technol. Innovation* **2020**, *18*, 100658. [CrossRef]

9. Gonçalves, N.P.F.; Paganini, M.C.; Armillotta, P.; Cerrato, E.; Calza, P. The effect of cobalt doping on the efficiency of semiconductor oxides in the photocatalytic water remediation. *J. Environ. Chem. Eng.* **2019**, *7*, 103475. [CrossRef]

10. Wang, R.; Ni, S.; Liu, G.; Xu, X. Hollow $CaTiO_3$ cubes modified by La/Cr co-doping for efficient photocatalytic hydrogen production. *Appl. Catal. B* **2018**, *225*, 139–147. [CrossRef]

11. Jiang, L.; Ni, S.; Liu, G.; Xu, X. Photocatalytic hydrogen production over Aurivillius compound Bi_3TiNbO_9 and its modifications by Cr/Nb co-doping. *Appl. Catal. B* **2017**, *217*, 342–352. [CrossRef]

12. Chen, P.-W.; Li, K.; Yu, Y.-X.; Zhang, W.-D. Cobalt-doped graphitic carbon nitride photocatalysts with high activity for hydrogen evolution. *Appl. Surf. Sci.* **2017**, *392*, 608–615. [CrossRef]

13. Regmi, C.; Kshetri, Y.K.; Pandey, R.P.; Kim, T.-H.; Gyawali, G.; Lee, S.W. Understanding the multifunctionality in Cu-doped $BiVO_4$ semiconductor photocatalyst. *J. Environ. Sci.* **2019**, *75*, 84–97. [CrossRef]

14. Habba, Y.; Capochichi-Gnambodoe, M.; Leprince-Wang, Y. Enhanced Photocatalytic Activity of Iron-Doped ZnO Nanowires for Water Purification. *Appl. Sci.* **2017**, *7*, 1185. [CrossRef]

15. Sultanov, F.R.; Daulbayev, C.; Bakbolat, B.; Zhurintayeva, A.; Daulbayev, O.; Mansurov, Z.A. Comparison of oil/water separating efficiency of oleophobic membranes based on fluorine containing and fluorine non-containing coatings. *RJC* **2019**, *12*, 1091–1097. [CrossRef]

16. Cheng, G.; Liu, X.; Song, X.; Chen, X.; Dai, W.; Yuan, R.; Fu, X. Visible-light-driven deep oxidation of NO over Fe doped TiO_2 catalyst: Synergic effect of Fe and oxygen vacancies. *Appl. Catal. B* **2020**, *277*, 119196. [CrossRef]

17. Ismael, M. Enhanced photocatalytic hydrogen production and degradation of organic pollutants from Fe(III) doped TiO_2 nanoparticles. *J. Environ. Chem. Eng.* **2020**, *8*, 103676. [CrossRef]

18. Zhang, H.; Chen, G.; Li, X. Synthesis and visible light photocatalysis water splitting property of chromium-doped $Bi_4Ti_3O_{12}$. *Solid State Ionics* **2009**, *180*, 1599–1603. [CrossRef]

19. Chen, Z.; Jiang, X.; Zhu, C.; Shi, C. Chromium-modified $Bi_4Ti_3O_{12}$ photocatalyst: Application for hydrogen evolution and pollutant degradation. *Appl. Catal. B* **2016**, *199*, 241–251. [CrossRef]

20. Zhu, H.; Fang, M.; Huang, Z.; Liu, Y.; Chen, K.; Guan, M.; Tang, C.; Zhang, L.; Wang, M. Novel chromium doped perovskites A_2ZnTiO_6 (A = Pr, Gd): Synthesis, crystal structure and photocatalytic activity under simulated solar light irradiation. *Appl. Surf. Sci.* **2017**, *393*, 348–356. [CrossRef]

21. Liu, J.; Hodes, G.; Yan, J.; Liu, S.F. Metal-doped Mo_2C (metal = Fe, Co, Ni, Cu) as catalysts on TiO_2 for photocatalytic hydrogen evolution in neutral solution. *Chin. J. Catal.* **2021**, *42*, 205–216. [CrossRef]

22. Nikhila, M.P.; John, D.; Pai, M.R.; Renuka, N.K. Cu and Ag modified mesoporous TiO_2 nanocuboids for visible light driven photocatalysis. *Nanostruct. Nano-Objects.* **2020**, *21*, 100420. [CrossRef]

23. Onwubiko, I.; Khan, W.S.; Subeshan, B.; Asmatulu, R. Investigating the effects of carbon-based counter electrode layers on the efficiency of hole-transporter-free perovskite solar cells. *Energ. Ecol. Environ.* **2020**, *5*, 141–152. [CrossRef]

24. Alharbi, A.R.; Alarifi, I.M.; Khan, W.S.; Swindle, A.; Asmatulu, R. Synthesis and characterization of electrospun polyacrylonitrile/graphene nanofibers embedded with $SrTiO_3$/NiO nanoparticles for water splitting. *J. Nanosci. Nanotechnol.* **2017**, *17*, 5294–5302. [CrossRef]

25. Asmatulu, R.; Shinde, M.A.; Alharbi, A.R.; Alarifi, I.M. Integrating graphene and C_{60} into TiO_2 nanofibers via electrospinning process for enhanced conversion efficiencies of DSSCs. *Macromol. Symp.* **2016**, *365*, 128–139. [CrossRef]

26. Sultanov, F.; Daulbayev, C.; Bakbolat, B.; Daulbayev, O.; Bigaj, M.; Mansurov, Z.; Kuterbekov, K.; Bekmyrza, K. Aligned composite $SrTiO_3$/PAN fibers as 1D photocatalyst obtained by electrospinning method. *Chem. Phys. Lett.* **2019**, *737*, 136821. [CrossRef]

27. Roy, P.K.; Bera, J. Formation of $SrTiO_3$ from Sr-oxalate and TiO_2. *Mater. Res. Bull.* **2005**, *40*, 599–604. [CrossRef]

28. Havlíček, K.; Svobodová, L.; Bakalova, T.; Lederer, T. Influence of electrospinning methods on characteristics of polyvinyl butyral and polyurethane nanofibres essential for biological applications. *Mater. Des.* **2020**, *194*, 108898. [CrossRef]

29. Huang, W.; Tong, Z.; Wang, R.; Liao, Z.; Bi, Y.; Chen, Y.; Ma, M.; Lyu, P.; Ma, Y. A review on electrospinning nanofibers in the field of microwave absorption. *Ceram. Int.* **2020**, in press. [CrossRef]

30. Guo, L.; Xie, N.; Wang, C.; Kou, X.; Ding, M.; Zhang, H.; Sun, Y.; Song, H.; Wang, Y.; Lu, G. Enhanced hydrogen sulfide sensing properties of Pt-functionalized α-Fe_2O_3 nanowires prepared by one-step electrospinning. *Sens. Actuators B* **2018**, *255*, 1015–1023. [CrossRef]

31. Zhao, J.; Lu, Q.; Wei, M.; Wang, C. Synthesis of one-dimensional α-Fe_2O_3/Bi_2MoO_6 heterostructures by electrospinning process with enhanced photocatalytic activity. *J. Alloys Compd.* **2015**, *646*, 417–424. [CrossRef]

32. Koo, B.-R.; Park, I.-K.; Ahn, H.-J. Fe-doped In_2O_3/α-Fe_2O_3 core/shell nanofibers fabricated by using a co-electrospinning method and its magnetic properties. *J. Alloys Compd.* **2014**, *603*, 52–56. [CrossRef]

33. Wu, L.; Shi, S.; Li, Q.; Zhang, X.; Cui, X. TiO_2 nanoparticles modified with 2D $MoSe_2$ for enhanced photocatalytic activity on hydrogen evolution. *Int. J. Hydrogen Energy* **2019**, *44*, 720–728. [CrossRef]

34. Yu, H.; Yan, S.; Li, Z.; Yu, T.; Zou, Z. Efficient visible-light-driven photocatalytic H_2 production over Cr/N-codoped $SrTiO_3$. *Int. J. Hydrogen Energy* **2012**, *37*, 12120–12127. [CrossRef]

35. Li, F.; Gu, Q.; Niu, Y.; Wang, R.; Tong, Y.; Zhu, S.; Zhang, H.; Zhang, Z.; Wang, X. Hydrogen evolution from aqueous-phase photocatalytic reforming of ethylene glycol over Pt/TiO_2 catalysts: Role of Pt and product distribution. *Appl. Surf. Sci.* **2017**, *391*, 251–258. [CrossRef]

36. López-Tenllado, F.J.; Hidalgo-Carrillo, J.; Montes, V.; Marinas, A.; Urbano, F.J.; Marinas, J.M.; Ilieva, L.; Tabakova, T.; Reid, F. A comparative study of hydrogen photocatalytic production from glycerol and propan-2-ol on M/TiO_2 systems (M = Au, Pt, Pd). *Catal. Today* **2017**, *280*, 58–64. [CrossRef]